RSC Sustainability

ROYAL SOCIETY OF CHEMISTRY

PAPER

View Article Online
View Journal | View Issue

Check for updates

Cite this: *RSC Sustainability*, 2025, **3**, 427

Zeolitic imidazolate framework improved vanadium ferrite: toxicological profile and its utility in the photodegradation of some selected antibiotics in aqueous solution

Adewale Adewuyi, *[a] Wuraola B. Akinbola,[ac] Chiagoziem A. Otuechere,[b] Adedotun Adesina,[b] Olaoluwa A. Ogunkunle,[c] Olamide A. Olalekan,[a] Sunday O. Ajibade[a] and Olalere G. Adeyemi[a]

Zeolitic imidazolate framework improved vanadium ferrite (VFe_2O_4@$_{mono}$ZIF-8) was prepared to purify a ciprofloxacin (CP), ampicillin (AP), and erythromycin (EY) contaminated water system *via* a visible light driven photocatalytic process. Furthermore, VFe_2O_4@$_{mono}$ZIF-8 was evaluated for its hepato-renal toxicity in Wistar rats to establish its toxicity profile. Characterization of VFe_2O_4@$_{mono}$ZIF-8 was performed with scanning electron microscopy (SEM), X-ray diffractometry (XRD), Fourier-transform infrared spectroscopy (FTIR), thermogravimetry evaluation (TGA), energy-dispersive X-ray microanalysis (EDX), and transmission electron microscopy (TEM). The VFe_2O_4@$_{mono}$ZIF-8 crystallite size determined by XRD is 34.32 nm, while the average particle size from the TEM image is 162.32 nm. The surface of VFe_2O_4@$_{mono}$ZIF-8 as shown in the SEM image is homogeneous having hexagonal and asymmetrically shaped particles. EDX results confirmed vanadium (V), iron (Fe), oxygen (O), carbon (C) and zinc (Zn) as the constituent elements. The bandgap energy is 2.18 eV. VFe_2O_4@$_{mono}$ZIF-8 completely (100%) photodegraded all the antibiotics (CP, AP and EY). In the 10th regeneration cycle, the degradation efficiency for CP was 95.10 ± 1.00%, for AP it was 98.60 ± 1.00% and for EY it was 98.60 ± 0.70%. VFe_2O_4@$_{mono}$ZIF-8 exhibited no significant changes in the plasma creatine, urea and uric acid levels of rats studied, suggesting healthy function of the studied kidneys. Furthermore, there was no significant effect on plasma electrolyte, sodium and potassium levels. The photocatalytic degradation capacity of VFe_2O_4@$_{mono}$ZIF-8 compared favorably with previous studies with minimal toxicity to the hepato-renal system, which suggests VFe_2O_4@$_{mono}$ZIF-8 as a potential resource for decontaminating antibiotic polluted water systems.

Received 1st November 2024
Accepted 27th November 2024

DOI: 10.1039/d4su00681j

rsc.li/rscsus

Open Access Article. Published on 05 Desemba 2024. Downloaded on 13/12/2025 21:30:58.
This article is licensed under a Creative Commons Attribution-NonCommercial 3.0 Unported Licence.

Sustainable spotlight

The detection of antibiotics in water is worrisome and there is a need to find a sustainable water treatment solution to completely (100%) remove them during wastewater purification. This research work addresses the sustainable development goal-6 (SDG-6) by proffering sustainable means for the purification of antibiotic-contaminated environmental drinking water sources. The aim is to provide safe clean water. Interestingly, zeolitic imidazolate framework improved vanadium ferrite (VFe_2O_4@monoZIF-8) in this study completely removes ciprofloxacin, ampicillin, and erythromycin from contaminated water. The study further examined the toxicity of VFe_2O_4@monoZIF-8. The photocatalytic degradation capacity of VFe_2O_4@monoZIF-8 compared favorably with previous studies with minimal toxicity to the hepato-renal system, which suggests VFe_2O_4@monoZIF-8 as a potential resource for decontaminating antibiotic polluted water.

1. Introduction

Despite the fact that antibiotics have saliently contributed to the control and treatment of diseases, their presence in potable water is prohibited. The indiscriminate use and poor unregulated environmental disposal of antibiotics contribute to their presence in environmental drinking water sources. Surface water systems are the most polluted among known environmental drinking water sources. Interestingly, studies have detected antibiotics in many surface water systems from several countries.[1–6] In fact, antibiotics have been uncovered in tap and bottled water in different countries.[7–11] Even when the antibiotics are present at low concentration, it is important to remove them from water; for example, metronidazole (an antibiotic) is

[a]*Department of Chemical Sciences, Faculty of Natural Sciences, Redeemer's University, Ede, Osun State, Nigeria. E-mail: walexy62@yahoo.com; Tel: +2348035826679*

[b]*Department of Biochemistry, Faculty of Basic Medical Sciences, Redeemer's University, Ede, Osun State, Nigeria*

[c]*Department of Chemistry, Obafemi Awolowo University, Ile-Ife, Nigeria*

© 2025 The Author(s). Published by the Royal Society of Chemistry

Open Access Article. Published on 05 Desemba 2024. Downloaded on 13/12/2025 21:30:58.
This article is licensed under a Creative Commons Attribution-NonCommercial 3.0 Unported Licence.

toxic, mutagenic and carcinogenic.[10] It is important that antibiotics are adequately quantified in water samples[12] to help in monitoring their presence in drinking water sources. This discovery of antibiotics in water is worrisome and there is a need to find a sustainable water treatment solution to remove them during the wastewater purification process.[6,11]

Most antibiotics are persistent in the environment and can metamorphose into forms that are toxic and may become harmful to human beings.[13,14] Although methods are known for decontaminating antibiotic-polluted water systems, many of these methods suffer from limitations such as insufficient removal of antibiotics, being expensive and production of toxic side products.[15] This research work is focused on overcoming these limitations by developing a water treatment resource that could completely eliminate antibiotics from water systems. Among the many known antibiotics, ciprofloxacin (CP), ampicillin (AP) and erythromycin (EY) are the most commonly detected antibiotics in drinking water, which may be due to their intemperate and indiscriminate use without medical prescriptions, since they are purchased over the counter in many poor nations.

This study focuses on the complete elimination of CP, AP, and EY from water because they are of serious concern due to their frequent detection in drinking water globally, especially in poor countries. The majority of the known wastewater treatment plants (WWTP) cannot completely remove them during the production of drinking water because the WWTPs were not designed to handle such emerging water micro-contaminants (CP, AP and EY). Interestingly, many studies have demonstrated that photocatalysis can remove organic pollutants from water by converting such pollutants to nontoxic low molecular weight molecules. Photocatalysts are capable of removing organic pollutants from water *via* an advanced oxidation process by generating highly reactive chemical species that attack the organic pollutants and convert them to less toxic smaller molecules.[10,16] Previously, titanium based photocatalyst were reported for antibiotic degradation with efficiency performance;[17] similarly, carbon quantum dot modified Bi_2MoO_6 demonstrated 88% efficiency towards the degradation of CP.[18] Although many photocatalysts have been produced, it is better to develop visible light active photocatalysts since visible light is abundantly and freely available, which makes the process affordable and cost-effective compared to using ultraviolet (UV) light active photocatalysts. UV light active photocatalysts require an additional UV light source for the photocatalytic process, which incurs an additional process cost. A study reported an efficiency of 55% for the degradation of CP using Bi_2MoO_6 as the photocatalyst.[19] Ion imprinting technology was adopted for immobilizing Fe^{2+}/Fe^{3+} onto TiO_2/fly-ash to produce a visible light active photocatalyst for purifying CP contaminated water.[20] Furthermore, a plasmonic photocatalyst (Ag/Ag_2MoO_4) demonstrated a 99% degradation of CP contaminated water.[21] A nanosheet heterojunction visible light active photocatalyst (Bi_3NbO_7) has shown an efficiency of 86% for removing CP from water.[22] Unfortunately, many of the reported photocatalysts do not have the capability to completely eliminate antibiotics of concern from water systems. Therefore, to overcome the limitation of insufficient removal of antibiotics from water, this work investigates the preparation of visible light sensitive photocatalysts for sufficient decontamination of antibiotic polluted water systems.

To develop an efficient photocatalyst, the current research work proposes vanadium ferrite (VFe_2O_4) as a visible light sensitive photocatalyst for removing CP, AP and EY from aqueous solutions. During the photocatalysis process, electron (e^-) and hole (h^+) pairs are produced to achieve the elimination of organic pollutants (in this case, antibiotics) in aqueous solutions; however, the e^-/h^+ pair may recombine to reduce the photocatalytic performance, which is a limitation to the water purification process.[23–26] To overcome the limitation of recombination of the e^-/h^+ pair, we conceptualize the incorporation of VFe_2O_4 in a carbon source. The carbon source may serve as a base for trapping the e^-/h^+ pair, which may help prevent the e^-/h^+ pair from recombining. Several materials are known to have the capacity to serve as carbon sources. Moreover, for the water purification process, water stable carbon base materials such as zeolitic imidazolate framework (ZIF-8) are preferred; therefore, to circumvent the limitation arising because of the recombination of e^-/h^+ pairs, ZIF-8 was utilized as the carbon source. Previous studies have reported the use of zirconium-based MOF materials as efficient resources for the removal of antibiotics from water systems.[27,28] Furthermore, MOF-based materials have also been reported for sensing antibiotics in water systems[29] with biomedical applications.[30–33] The toxicity profiles of the many photocatalysts known are uninvestigated. The lack of information on the toxicity profile of photocatalysts used in water treatment has limited their use in large scale water purification. It is a necessity to establish the safety profile of photocatalysts when used in water purification to better understand the human safety exposure limit in case the photocatalyst leaches into water during treatment.

To assess the complete elimination of antibiotics from water, this study aims to incorporate VFe_2O_4 into ZIF-8 to produce $VFe_2O_4@_{mono}$ZIF-8 as a monolithic photocatalyst for the degradation of CP, AP and EY. Apart from serving as a carbon source, the inclusion of ZIF-8 to form a monolithic photocatalyst ($VFe_2O_4@_{mono}$ZIF-8) additionally aids in the recovery of particles of VFe_2O_4 from solution. Furthermore, this study aims to investigate the safety profile of $VFe_2O_4@_{mono}$ZIF-8 as a photocatalyst by subjecting $VFe_2O_4@_{mono}$ZIF-8 to animal studies. To date, information on the synthesis and application of VFe_2O_4@ZIF-8 as a photocatalyst for water treatment is limited. Moreover, there is no information on the toxicity profile of $VFe_2O_4@_{mono}$ZIF-8.

2. Materials and methods

2.1. Materials

Zinc dinitrate ($Zn(NO_3)_2 \cdot 6H_2O$), 1-chloro-2,4-di nitrobenzene (CDNB), hydrochloric acid (HCl), sodium chloride (NaCl), polyvidone (PVP), iron(III) chloride ($FeCl_3 \cdot 6H_2O$), thiobarbituric acid (TBA), sodium hydroxide (NaOH), 2-methyl-1*H*-imidazole ($CH_3C_3H_2N_2H$), ammonia solution (NH_4OH), vanadium(III) chloride (VCl_3), 2,2-diphenyl-1-picrylhydrazyl ($C_{18}H_{12}N_5O_6$),

© 2025 The Author(s). Published by the Royal Society of Chemistry

Open Access Article. Published on 05 Desemba 2024. Downloaded on 13/12/2025 21:30:58. This article is licensed under a Creative Commons Attribution-NonCommercial 3.0 Unported Licence.

methanol (CH_3OH), epinephrine ($C_9H_{13}NO_3$) methyl trichloride (TM), diammonium oxalate (DO), 2-propanol (2P), dimethyl sulfoxide (DMSO), CP, AP, EY, 5′,5′-dithiobis-(2-nitrobenzoic acid), dimethylsulfoxide (DMSO) and ethanol ($C2H_5OH$) were procured from Aldrich Chemical Co., England.

2.2. Synthesis of VFe_2O_4 particles

Particles of VFe_2O_4 were synthesized by mixing aqueous solutions of 0.2 M VCl_3, 0.4 M $FeCl_3 \cdot 6H_2O$ and PVP at 80 °C for 60 min in a 1 L beaker. The solution pH of the reacting mixture was increased to a pH of 10 by adding NH_4OH solution and stirred for another 60 min. After cooling to 303 K, the reaction solution was filtered and the residue was washed many times with deionized H_2O and C_2H_5OH. The washed residue was dried at 105 °C in an oven for 5 h and kept in a furnace at 550 °C for 18 h.

2.3. Synthesis of VFe_2O_4@$_{mono}$ZIF-8

Methanol solutions of 0.985 mmol $Zn(NO_3)_2 \cdot 6H_2O$ and 0.985 mmol $CH_3C_3H_2N_2H$ (containing 50 mg of VFe_2O_4 particles) were separately sonicated at 303 K for 30 min. The sonicated methanol solutions of $Zn(NO_3)_2 \cdot 6H_2O$ and $CH_3C_3H_2N_2H$ + VFe_2O_4 were combined and stirred at 120 rpm for 15 min (303 K). The product formed was separated by centrifugation at 6000 rpm (20 min) and washing 3 times with C_2H_5OH. The product obtained was dried at 303 K overnight.

2.4. Characterization of VFe_2O_4@$_{mono}$ZIF-8

VFe_2O_4@$_{mono}$ZIF-8 was analyzed on Fourier transform infrared spectroscopy (FTIR) while the thermogravimetric measurement was conducted on a TGA/DSC Star^e. The X-ray diffraction pattern was obtained using a diffractometer (at 2θ from 5–90°). The surface structure was observed by scanning electron microscopy (SEM), which was coupled with energy-dispersive X-ray spectroscopy (EDX) to determine the constituent element. The surface properties were further checked using transmission electron microscopy (TEM), while activity under UV/visible light was recorded on a UV-visible spectrophotometer.

2.5. Photocatalytic degradation of CP, AP and EY by VFe_2O_4@$_{mono}$ZIF-8

Photodegradation of CP, AP, and EY *via* VFe_2O_4@$_{mono}$ZIF-8 was achieved by subjecting antibiotic (CP, AP or EY) solution (50 mL, 10.00 mg L^{-1}) to xenon, 150 W, 550 nm irradiation for 200 min under stirring at 120 rpm in the presence of VFe_2O_4@$_{mono}$ZIF-8 (0.005 g). Samples were withdrawn at intervals and examined with a PerkinElmer UV-visible spectrophotometer to determine the extent of photocatalytic degradation or photocatalytic degradation capacity of VFe_2O_4@$_{mono}$ZIF-8. The withdrawn samples were read at predetermined λ_{max}: λ_{max} = CP_{271nm}, AP_{420nm} and EY_{285nm}. To optimize the photodegradation process, antibiotic aqueous solution concentration was varied from 2.00–10.00 mg L^{-1}, the weight of VFe_2O_4@$_{mono}$ZIF-8 was varied from 0.001 to 0.05 g and antibiotic aqueous solution pH was varied from pH 2 to 10. Under the established optimized process conditions, the experiment was conducted skiving off the xenon, 150 W, irradiation to probe adsorption existence during the photocatalytic degradation process. All the experiments were conducted in triplicate. The photocatalytic degradation efficiency was determined as:

$$\text{Degradation efficiency}(\%) = 100 \times \left(1 - \frac{C_t}{C_0}\right) \quad (1)$$

The percentage removal achieved by VFe_2O_4@$_{mono}$ZIF-8 towards the antibiotics for the experiment conducted without supplying visible light was determined as:

$$\%\ \text{removal} = \frac{(C_0 - C_e)}{C_0} \times 100 \quad (2)$$

In eqn (1) and (2), C_0, C_t and C_e represent the initial, time and equilibrium concentrations of the test solution, respectively.

2.6. Determination of the contribution from ROS in the photodegradation process

The mechanism describing the antibiotic photodegradation by VFe_2O_4@$_{mono}$ZIF-8 was investigated by studying the role of ROS in the process by adding 1 mM of specific ROS scavenger to the photocatalytic degradation medium. In this study, DO scavenged h^+ while the hydroxyl radical ($OH^\bullet$) was scavenged by 2P. TM was responsible for scavenging the superoxide ion radical ($^\bullet O_2^-$). The role of ROS was probed keeping the process parameters as: antibiotic test solution concentration = 10.00 mg L^{-1}, VFe_2O_4@$_{mono}$ZIF-8 weight = 0.005 g, antibiotic aqueous solution pH = 7.2, stirring speed = 120 rpm and photodegradation time = 160 min. The experiments were conducted in triplicate (with and without the scavenger for comparison).

2.7. Regeneration of VFe_2O_4@$_{mono}$ZIF-8 for reuse

VFe_2O_4@$_{mono}$ZIF-8 was regenerated *via* a solvent regeneration process using deionized H_2O, 0.1 M HCl, DMSO or a mixture of DMSO and 0.1 M HCl (1 : 3) as regeneration solvent. After each 160 min of photodegradation, VFe_2O_4@$_{mono}$ZIF-8 was recovered from the medium by 20 min centrifugation at 5500 rpm. The recovered VFe_2O_4@$_{mono}$ZIF-8-Antibiotic (CP/AP/EY) was dispersed in the regeneration solvent (20 mL) and sonicated for 30 min before centrifuging at 5500 rpm for 20 min. The obtained VFe_2O_4@$_{mono}$ZIF-8 was dried for 3 h at 378 K in an oven to activate it for reuse. The regeneration process was repeated in the 10th cycles. Samples were taken at each cycle and analyzed by atomic absorption spectroscopy (AAS) with a graphite tube atomizer to check whether VFe_2O_4@$_{mono}$ZIF-8 leached into the medium as photodegradation took place. VFe_2O_4@$_{mono}$ZIF-8 was recharacterized by XRD and FTIR after the 10th cycle to validate any changes in its structure.

2.8. Toxicity profiling of VFe_2O_4@$_{mono}$ZIF-8

Healthy Wistar rats weighing 150–200 g were administered VFe_2O_4@$_{mono}$ZIF-8 to investigate its hepato-renal effect. To

Open Access Article. Published on 05 Desemba 2024. Downloaded on 13/12/2025 21:30:58. This article is licensed under a Creative Commons Attribution-NonCommercial 3.0 Unported Licence.

achieve this, the rats were divided into 3 different groups (n = 6). The rats were fed with a standard pelleted diet (Ladokun FeEDX, Ibadan, Nigeria) and housed under relative humidity (70–80%) and a temperature of 298 K for 12 h day/night cycles. The animals received care as stipulated by Redeemer's University research and ethics committee. VFe_2O_4@$_{mono}$ZIF-8 was administered for fourteen days as follows:

- Group A: control experiment (rats fed with 0.9% saline).
- Group B: rats fed with VFe_2O_4@$_{mono}$ZIF-8 ((1 mg per kg body weight), orally, once daily).
- Group C: rats fed with VFe_2O_4@$_{mono}$ZIF-8 ((2 mg per kg body weight), orally, once daily).

Each group was steadily monitored daily for any symptoms and clinical signs of toxicity. The rats were cervically dislocated 24 h after the last administration of VFe_2O_4@$_{mono}$ZIF-8. Blood was obtained from experimental rats by venipuncture and collected into EDTA bottles. The blood collected was subsequently centrifuged (4000 rpm, 10 min) to obtain the plasma and freeze stored (−20 °C) until further analysis. After the sacrifice, the liver and kidneys were harvested, cleaned and kept in ice-cold sucrose solution (0.25 M). The organs were blotted before being separately homogenized (0.1 M phosphate buffer solution) at pH 7.4. Post-mitochondrial fractions were obtained after centrifuging the homogenates at 10 000 rpm for 20 min at 4 °C. The supernatants were frozen-stored at −20 °C until required for analysis. Albumin, aspartate aminotransferase (AST), creatinine, alanine aminotransferase (ALT), total bilirubin, triglycerides, calcium, sodium and potassium were determined using Randox kits.[34] All animal care and experimental etiquette were executed according to the approved guidelines set by the Redeemer's University Committee on Ethics for Scientific Research. The approved code for this study is RUN/REC/2022/007.

2.9. Histological and gross examination

The harvested liver and kidney tissues were fixed with formalin (10%). They were dehydrated in alcohol (70–100%) and embedded in paraffin (4 °C; 15 min) before being cut into sections (5 μm) using a rotary microtome. The slides were oven-dried at 37 °C for 12 h and processed for periodic acid–Schiff (PAS) counter-staining. The specimens were examined for morphological alterations using a light microscope.[35]

2.10. Statistical analyses

Data were statistically treated using one-way analysis of variance (ANOVA) and Dunnet's *post hoc* test on Graph Pad Prism 8 software. Data with a p-value < 0.05 are regarded as significant.

3. Results and discussion

3.1. Synthesis and characterization of VFe_2O_4@$_{mono}$ZIF-8

The FTIR result (Fig. 1a) showed peaks suggesting the synthesis of VFe_2O_4@$_{mono}$ZIF-8. The broad signal at 3421 cm^{-1} is the overlapping vibrations of N–H and O–H stretches arising from the imidazole structure of VFe_2O_4@$_{mono}$ZIF-8 and adsorbed water molecules.[36–38] The peaks at 3092 and 2921 cm^{-1} were the C–H stretches of the aromatic ring and alkanes, respectively. The band appearing at 1653 cm^{-1} was attributed to the O–H bond of the adsorbed water molecule resonating the stretch at 3421 cm^{-1}. The stretches of C=N of the imidazole structure and C=C of the aromatic ring were seen at 1648 and 1582 cm^{-1}, respectively. The signal corresponding to the C–N stretch appeared at 1297 cm^{-1} while the O–Fe–O vibration was at 1110 cm^{-1}. The O–V–O and V–Fe vibration frequencies appeared at 983 and 962 cm^{-1}, respectively. The signal at 910 cm^{-1} was assigned to the C–N bend. The Fe–O and Zn–N signals appeared at 641 and 624 cm^{-1}, respectively, while the V–O vibration appeared at 501 cm^{-1}.

The thermal stability of VFe_2O_4@$_{mono}$ZIF-8 is revealed in Fig. 1b, which shows five distinct mass losses. The loss in the range 55 to 137 °C suggests the loss of water molecules and other adsorbed small molecules. This confirms the FTIR results at 3421 cm^{-1} suggesting the O–H stretch of adsorbed water molecules. The second loss at 137 to 401 °C suggests the decomposition of the imidazole structure in the molecule of VFe_2O_4@$_{mono}$ZIF-8, which may be accompanied by loss of small molecules like CO_2, NH_3, and H_2O. The loss from 401 to 503 °C may account for the dehydration of the OH group with the formation of oxides of metal because of intra- and intermolecular transfer interactions.[39,40] The observation of mass loss from 503 to 614 °C may be due to the continuous decomposition and phase change occurring in the structure of

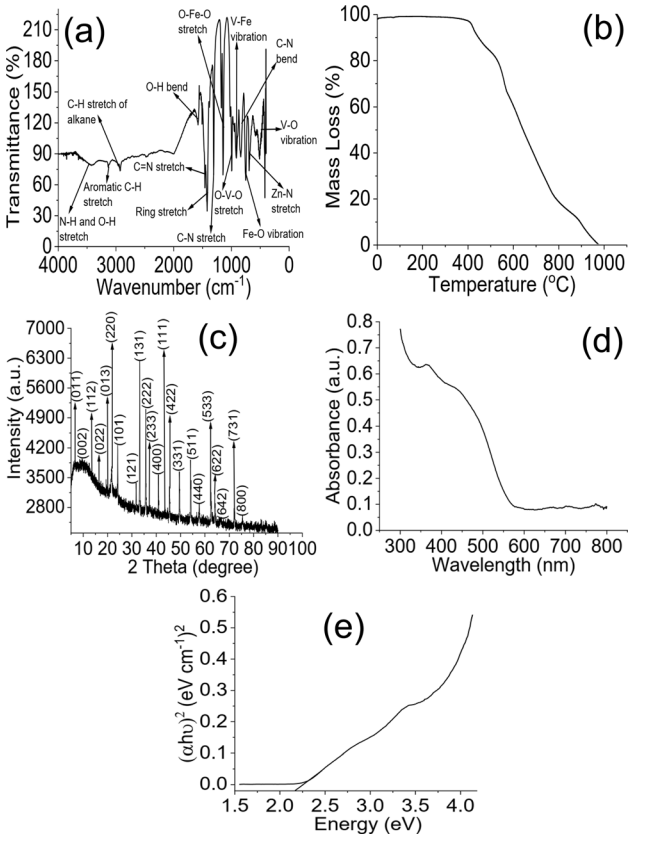

Fig. 1 FTIR (a), TGA (b), XRD (c), UV-visible (d) and Tauc plot (e) of VFe_2O_4@$_{mono}$ZIF-8.

© 2025 The Author(s). Published by the Royal Society of Chemistry

Open Access Article. Published on 05 Desemba 2024. Downloaded on 13/12/2025 21:30:58.
This article is licensed under a Creative Commons Attribution-NonCommercial 3.0 Unported Licence.

VFe_2O_4@$_{mono}$ZIF-8, while the loss above from 614 °C may be due to structural collapse and carbonization of VFe_2O_4@$_{mono}$-ZIF-8.[41] The X-ray diffraction pattern of VFe_2O_4@$_{mono}$ZIF-8 (Fig. 1c) showed signals spacing at 2θ corresponding to (011), (002), (112), (022), (013), (220), (101), (121), (131), (222), (233), (400), (111), (422), (331), (511), (440), (533), (622), (642), (731) and (800). The crystallite size (D) of VFe_2O_4@$_{mono}$ZIF-8 was determined from the X-ray wavelength, λ (1.5406 Å), constant, K (0.89), width of the diffraction pattern (β) and Bragg's angle (θ) as defined below:[42,43]

$$D = \frac{K\lambda}{\beta \cos \theta} \quad (3)$$

The D value obtained for VFe_2O_4@$_{mono}$ZIF-8 is 34.32 nm. The value is smaller compared to the value range (37–45 nm) revealed for some ferrite molecules,[44] suggesting the potential of VFe_2O_4@$_{mono}$ZIF-8 being a catalyst.[45]

The UV-visible analysis of VFe_2O_4@$_{mono}$ZIF-8 (Fig. 1d) revealed sensitivity in response to the visible region of light, which supports the fact that VFe_2O_4@$_{mono}$ZIF-8 can serve as a visible light active photocatalyst. This is the reason for using VFe_2O_4@$_{mono}$ZIF-8 in this study for the photocatalytic degradation of CP, AP and EY. Moreover, being active in visible light suggests that there may be no need to purchase an external source of light to activate VFe_2O_4@$_{mono}$ZIF-8 for the photocatalytic process since visible light is abundant in nature. The Tauc plot (Fig. 1e) from the data generated from the UV-visible activity of VFe_2O_4@$_{mono}$ZIF-8 could describe the energy band gap (E_g) from the light frequency ($h\nu$) and proportionality constant (A), as:

$$(\propto h\nu)^2 = A(h\nu - E_g) \quad (4)$$

The Tauc plot revealed the E_g of VFe_2O_4@$_{mono}$ZIF-8 to be 2.18 eV, which is within the range for visible light active

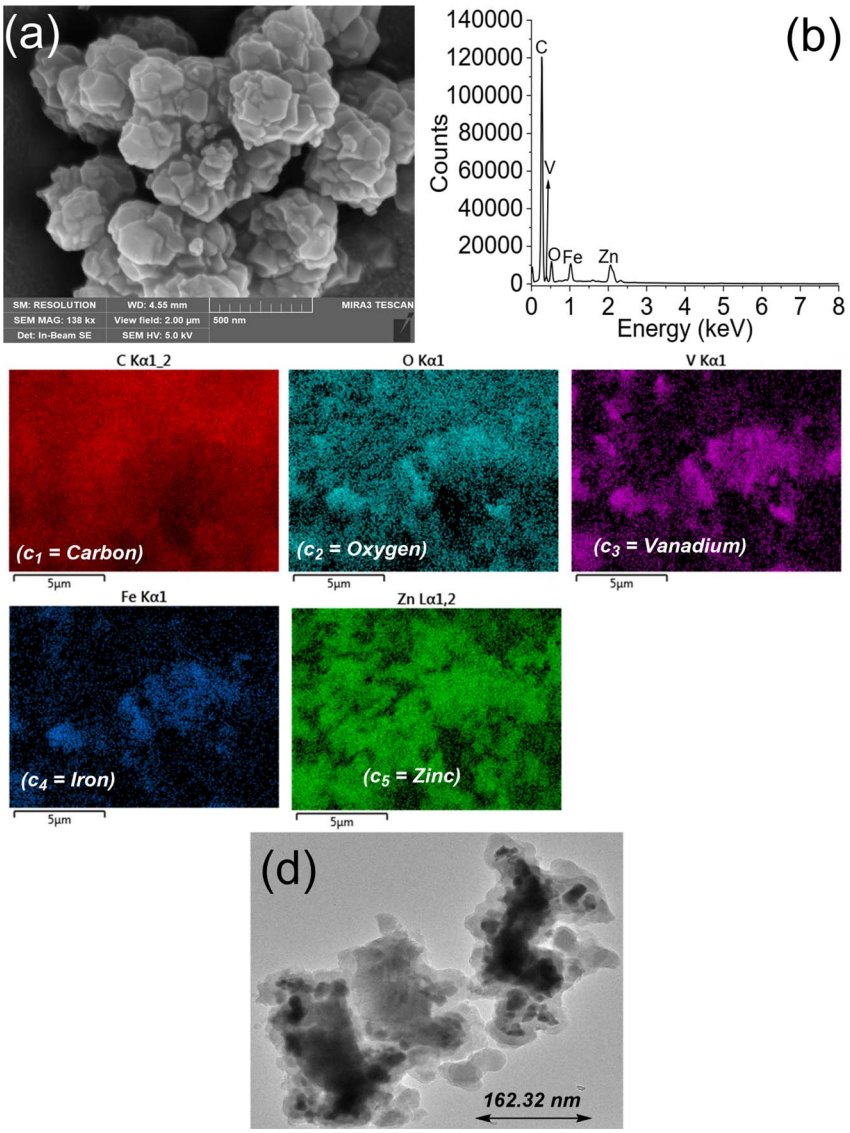

Fig. 2 SEM of VFe_2O_4@$_{mono}$ZIF-8 (a), EDX of VFe_2O_4@$_{mono}$ZIF-8 (b), elemental mapping of VFe_2O_4@$_{mono}$ZIF-8 (c) and TEM of VFe_2O_4@$_{mono}$ZIF-8 (d).

Open Access Article. Published on 05 Desemba 2024. Downloaded on 13/12/2025 21:30:58.
This article is licensed under a Creative Commons Attribution-NonCommercial 3.0 Unported Licence.

photocatalysts.[46,47] The optical macroscopic properties of VFe_2O_4@$_{mono}$ZIF-8 from the UV-visible absorption data may help in understanding the particle size dispersion and filling factor of VFe_2O_4@$_{mono}$ZIF-8;[48–50] however, this study confirmed the direct electronic transition of bulk VFe_2O_4@$_{mono}$ZIF-8 by E_g. The SEM results (Fig. 2a) revealed the surface of VFe_2O_4@$_{mono}$ZIF-8 to be homogeneous with hexagonal and asymmetrically shaped particles. The elemental composition from EDX (Fig. 2b) includes V, C, O, Zn and Fe as buttressed by the elemental mapping result (Fig. 2c$_{1-5}$). TEM results (Fig. 2d) revealed a morphology of VFe_2O_4@$_{mono}$ZIF-8 with particles that appear flaky and a few oval shaped particles. TEM results confirmed the average particle size of VFe_2O_4@$_{mono}$ZIF-8 to be 162.32 nm.

3.2. Photodegradation of antibiotics by VFe_2O_4@$_{mono}$ZIF-8

VFe_2O_4@$_{mono}$ZIF-8 achieved a complete removal (100%) of the evaluated antibiotics from solution (Fig. 3a). The complete removal was attained at different irradiation times. The degradation of CP, AP and EY plateaued at 80, 140 and 160 min of irradiation, respectively. The degradation was studied at different solution concentrations varying from 1 to 10 mg L^{-1} (Fig. 3b). The study showed a complete removal of the antibiotics even at these concentrations, which are higher than the actual concentrations at which the antibiotics have been detected in environmental drinking water source samples.[4] The VFe_2O_4@$_{mono}$ZIF-8 loading (Fig. 3c) showed a steady increase in degradation efficiency as loading increased from 0.04 to 0.2 g L^{-1} for CP, AP and EY, which may be ascribed to an increase in the surface area promoting the generation of e^-/h^+ pairs required for the photodegradation. The efficiency remained constant from a loading of 0.2 to 0.32 g L^{-1} except for EY (0.2 to 0.4 g L^{-1}). However, increasing the weight above 0.32 g L^{-1} for CP and AP or 0.4 g L^{-1} for EY led to a decrease in the degradation efficiency of VFe_2O_4@$_{mono}$ZIF-8, which may be due to the reduction in photoillumination resulting from the cloudiness of the reaction medium.[51] The effect of the test solution pH on the performance of VFe_2O_4@$_{mono}$ZIF-8 is shown in Fig. 3d. The degradation process is favored as pH moves towards neutrality. The preferred solution pH for optimum photodegradation performance is 7.2. Unfortunately, the performance of VFe_2O_4@$_{mono}$ZIF-8 reduced as the solution pH increased towards alkalinity. This observation may be due to the fact that the generation of ROS becomes favored as the solution pH moves towards neutrality, whereas as the pH tends towards alkalinity, smaller amounts of active ROS are available to promote the degradation process.

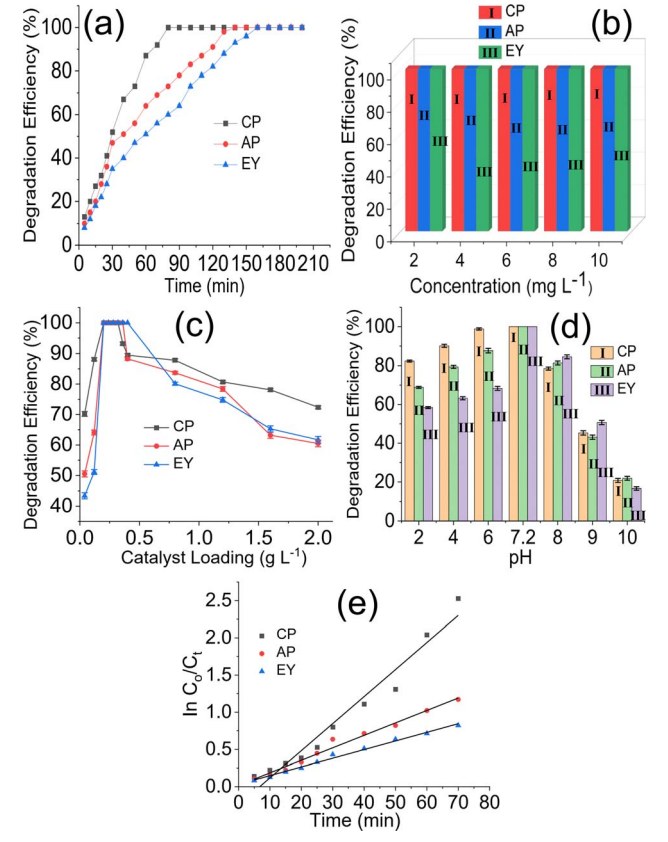

Fig. 3 Time dependent degradation of CP, AP and EY by VFe_2O_4@$_{mono}$ZIF-8 under visible light irradiation at an antibiotic concentration of 10.00 mg L^{-1} (a), effect of solution concentration on the degradation efficiency of VFe_2O_4@$_{mono}$ZIF-8 towards CP, AP and EY (b), effect of catalyst loading on the degradation efficiency of VFe_2O_4@$_{mono}$ZIF-8 towards CP, AP and EY (c), effect of solution pH on the degradation efficiency of VFe_2O_4@$_{mono}$ZIF-8 towards CP, AP and EY (d) and plot of ln C_0/C_t *versus* irradiation time for the degradation of CP, AP and EY at 10.00 mg L^{-1} (e).

The data generated from the optimized process parameter were subjected to pseudo-1st-order kinetic analysis. The process rate constant (k) was estimated from the initial concentration (C_0) and time t concentration (C_t) as expressed below:

$$\ln\left(\frac{C_0}{C_t}\right) = kt \quad (5)$$

The value of k was obtained from the plot of ln C_0/C_t *vs.* time (t) for light irradiation (Fig. 3e). The obtained k values could be described as: CP (0.0364 min^{-1}) > AP (0.0168 min^{-1}) > EY (0.0116 min^{-1}), suggesting that the process was fastest for CP compared to AP and EY. This may be related to the molecular weight, CP (331.347 g mol^{-1}) < AP (349.41 g mol^{-1}) < EY (733.937 g mol^{-1}), indicating that the degradation rate becomes fastest with the antibiotic having the least molecular weight (CP). This explanation is apparent in the degradation time, which is CP (80 min) < AP (140 min) < EY (160 min), indicating that photodegradation was achieved more quickly for antibiotics with low molecular weights.

3.3. Determination of the contribution from ROS in the photodegradation process

The interaction between VFe_2O_4@$_{mono}$ZIF-8 and the antibiotics was described by studying the ROS involved in the reaction (Fig. 4a). The involvement of ROS was evaluated by scavenging the ROS during the process. Studies have shown that during the photodegradation process, four reactive species are known and the process may involve all, any or some of the reactive species.[52–54] When 2P was included in the reaction medium to

© 2025 The Author(s). Published by the Royal Society of Chemistry

Open Access Article. Published on 05 Desemba 2024. Downloaded on 13/12/2025 21:30:58.
This article is licensed under a Creative Commons Attribution-NonCommercial 3.0 Unported Licence.

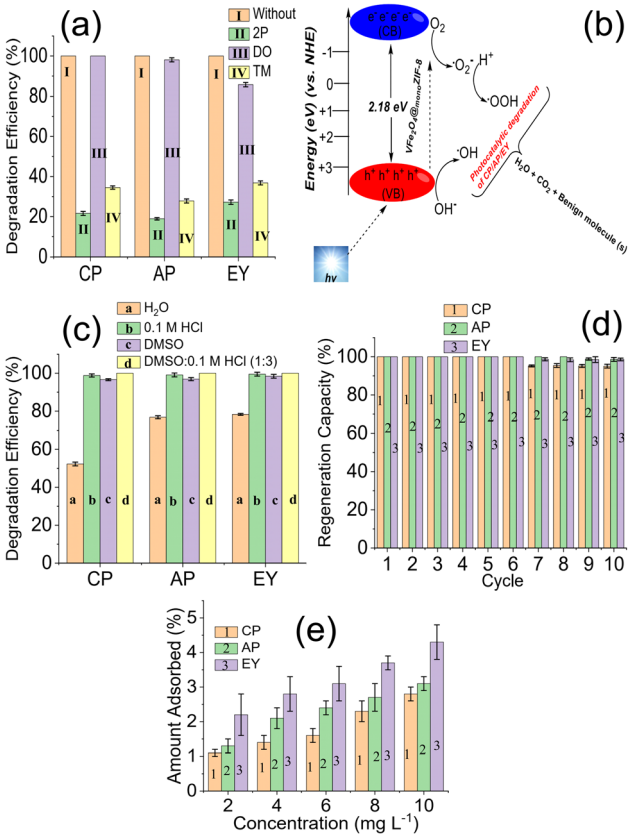

Fig. 4 Degradation efficiency of VFe_2O_4@$_{mono}$ZIF-8 towards CP, AP and EY with and without ROS scavengers (a), proposed mechanism for the photodegradation of CP, AP and EY by VFe_2O_4@$_{mono}$ZIF-8 (b), photodegradation efficiency of VFe_2O_4@$_{mono}$ZIF-8 after treatment with different solvent systems (c), regeneration capacity of VFe_2O_4@$_{mono}$ZIF-8 towards CP, AP and EY in different treatment cycles (d) and amounts of CP, AP and EY adsorbed by VFe_2O_4@$_{mono}$ZIF-8 in the absence of light (e).

scavenge $OH^{\bullet}$, the degradation efficiency reduced, which suggests that $OH^{\bullet}$ is involved in the process. A similar observation was made when h^+ and e^- were scavenged except for CP when h^+ was scavenged. The efficiency was least when $OH^{\bullet}$ was scavenged, indicating that it played the most important role during the photodegradation, while the highest degradation efficiency was obtained when h^+ was scavenged, indicating that h^+ played the least important role during the process. The contributions from the ROS for the degradation could be described as $OH^{\bullet} > {}^{\bullet}O_2^- > h^+$. Many studies have shown the mechanism to involve the emergence of e^-/h^+ pairs at the valence band of the catalyst (VFe_2O_4@$_{mono}$ZIF-8) when exposed to visible light.[55–57] The e^- migrates to the conduction band while the h^+ is in the valence band. The h^+ interacts with the water molecule to generate the $OH^{\bullet}$ radical while the e^- interacts with O_2 molecules in the H_2O to release the ${}^{\bullet}O_2^-$ radicals. The radicals produced collide with the molecules of the antibiotics to initiate a continuous degradation process, as described in Fig. 4b. One major disadvantage of the process is the e^-/h^+ pair recombination, which reduces or limits the photodegradation performance. This recombination was mitigated in this study by the introduction of a carbon source involving the $_{mono}$ZIF-8 structure. Interestingly, the degradation process was continuous, attaining a 100% removal of the antibiotics. The inclusion of $_{mono}$ZIF-8 did not only help prevent the recombination of the e^-/h^+ pair but also helped in the catalyst recovery from solution since VFe_2O_4@$_{mono}$ZIF-8 remained a monolith throughout the process.

3.4. Regeneration of VFe_2O_4@$_{mono}$ZIF-8 for reuse

The regeneration of VFe_2O_4@$_{mono}$ZIF-8 was evaluated by solvent regeneration. First, the solvents were screened as shown in Fig. 4c to identify the most suitable solvent for the regeneration. The evaluation revealed that a mixture of DMSO and 0.1 M HCl (1 : 3) was the best solvent for the regeneration. Further regeneration of VFe_2O_4@$_{mono}$ZIF-8 was achieved using a mixture of DMSO and 0.1 M HCl (1 : 3). The catalyst regeneration cycle was up to the 10th cycle. The regeneration of VFe_2O_4@$_{mono}$ZIF-8 was steady and 100% up to the 6th cycle for CP, AP and EY except for AP, which maintained a 100% regeneration capacity up to the 8th cycle (Fig. 4d). In the 10th regeneration cycle, the degradation efficiency for CP was 95.10 ± 1.00%, for AP it was 98.60 ± 1.00%, and for EY it was 98.60 ± 0.70%. The results from the skiving off of light revealed adsorption taking place during the process but with less that >5% efficiency demonstrated by VFe_2O_4@$_{mono}$ZIF-8, as shown in Fig. 4e. The results from the AAS showed no leaching of VFe_2O_4@$_{mono}$ZIF-8 into the solution at the cycles analyzed, which suggests the stability of the catalyst. Furthermore, the FTIR (Fig. 5a) and XRD (Fig. 5b) of VFe_2O_4@$_{mono}$ZIF-8 before and after the degradation did not show any phase change of defects in the structure of VFe_2O_4@$_{mono}$ZIF-8, suggesting the good stability of VFe_2O_4@$_{mono}$ZIF-8 through the process.

The degradation capacity exhibited by VFe_2O_4@$_{mono}$ZIF-8 was compared with that of other photocatalysts reported in the literature (Table 1). VFe_2O_4@$_{mono}$ZIF-8 compared favorably with published reports demonstrating complete removal of the antibiotics and a regeneration capacity above 95%. The degradation capacity of VFe_2O_4@$_{mono}$ZIF-8 towards CP is higher than the values obtained for CeNTs,[60] CeO_2/ZnO[65] and ZnO/g-C_3N_4.[66] Its performance towards AP is better than that of $Ru/WO_3/ZrO_2$ with

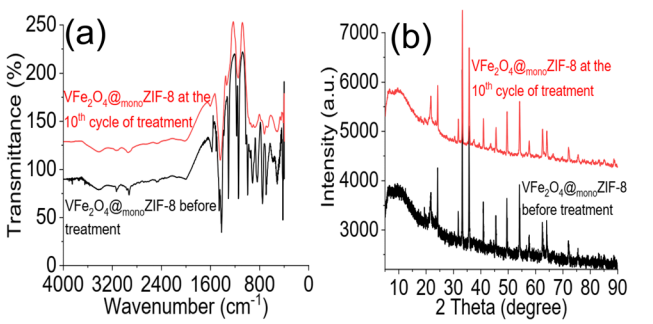

Fig. 5 FTIR of VFe_2O_4@$_{mono}$ZIF-8 before photocatalytic degradation and in the 10th cycle of the photocatalytic degradation process (a) and XRD of VFe_2O_4@$_{mono}$ZIF-8 before photocatalytic degradation and in the 10th cycle of photocatalytic degradation (b).

© 2025 The Author(s). Published by the Royal Society of Chemistry

Open Access Article. Published on 05 Desemba 2024. Downloaded on 13/12/2025 21:30:58. This article is licensed under a Creative Commons Attribution-NonCommercial 3.0 Unported Licence.

Table 1 Comparison between the photodegradation performance of VFe_2O_4@$_{mono}$ZIF-8 and previously reported photocatalysts[a]

Material	ANB	DEF (%)	LS	CL (g L^{-1})	Conc (mg L^{-1})	Stability (%)	Reference
$ZnFe_2O_4$@chitosan	CP	99.80	Xe lamp (150 W)	1.00	5.00	97.60 (15th cycle)	45
Cu_xO/MOF	CP	92.00	VL	0.50	15.00	>85 (6th cycle)	58
NCuTCQD	CP	100	Xe lamp	0.80	20.00	93.00 (6th cycle)	59
CeO_2	CP	61.00	UV-B light	0.05	10.00	—	60
CeNTs	CP	89.00	UV-B light	0.05	10.00	—	60
ZIF-8/SOD	CP	99.80	Hg lamp	0.16	10.00	60.00 (3rd cycle)	61
Fe_3O_4/Bi_2WO_6	CP	99.70	VL	3.00	10.00	95.00 (5th cycle)	62
MMT/$CuFe_2O_4$	CP	83.75	UV light	0.78	32.50	—	63
Cu_2O/MoS_2/rGO	CP	55.00	Halogen lamp	0.30	10.00	—	64
CeO_2/ZnO	CP	60.00	200 W Hg–Xe lamp	0.25	15.00	>50 (4th cycle)	65
ZnO/g-C_3N_4	CP	93.80	VL	0.05	20.00	89.80 (3rd cycle)	66
CeO_2–Ag/AgBr	CP	93.05	Xe lamp (300 W)	2.50	10.00	93.05 (4th cycle)	67
R. gordoniae rjjtx-2	EY	75.00	—	—	100.00	—	68
Znpc–TiO_2	EY	74.21	VL	0.40	1×10^{-5} M	68.59 (5th cycle)	69
TiO_2	EY	31.57	VL	0.40	1×10^{-5} M		69
CNCS	EY	81.02	UVc lamps (35 W)	0.50	50.00	—	70
$Ti_{1-x}Sn_xO_2$	EY	67.00	Sunlight	1.50	50.00	50.00 (12th cycle)	71
$NiFe_2O_4$@chitosan	EY	100.00	150 W Xe light	1.00	5.00	83.30 (15th cycle)	72
$ZnFe_2O_4$@chitosan	EY	83.20	VL	1.00	5.00	95.00 (15th cycle)	45
MWCNTs–$CuNiFe_2O_4$	AP	100.00	UV (36 W)	0.50	25.00	93.72 (8th cycle)	73
Ru/WO_3/ZrO_2	AP	96.00	Xe lamp (150 W)	1.00	50.00	92.00 (2nd cycle)	74
FeSi@MN	AP	70.00	Sunlight	0.60	100.00	63.00 (4th cycle)	75
VFe_2O_4@$_{mono}$ZIF-8	CP	100	VL (150 W Xe light)	0.20	10.00	95.10 (10th cycle)	This study
	AP	100		0.20	10.00	98.60 (10th cycle)	
	EY	100		0.20	10.00	98.60 (10th cycle)	

[a] MMT/$CuFe_2O_4$ = ferrite copper nanoparticles on montmorillonite, — = not reported, Conc = concentration of antibiotic, MWCNTs–$CuNiFe_2O_4$ = nickel–copper ferrite nanoparticles on multi-walled carbon nanotubes, AP = ampicillin, LS = light illumination source, NCuTCQD = carbon quantum dots decorated on N–Cu co-doped titania, CL = catalyst loaded, ZIF-8/SOD = zeolitic imidazolate framework/sodalite zeolite, Znpc–TiO_2 = zinc phthalocyanine modified TiO_2 nanoparticles, CNCS = cellulose nanocrystals, DEF = degradation efficiency, CP = ciprofloxacin, VL = visible light, and antibiotic = ANB.

better regeneration capacity.[74] The synthesis of VFe_2O_4@$_{mono}$ZIF-8 is simple and can be easily regenerated by nontoxic solvent systems for reuse. The capacity expressed by VFe_2O_4@$_{mono}$ZIF-8 towards EY is higher than those of Znpc–TiO_2 (ref. 69) and γ-Fe_2O_3/SiO_2.[76] The study revealed VFe_2O_4@$_{mono}$ZIF-8 to be a promising photocatalyst with capacity that compared favorably with other previously reported photocatalysts in the literature.

3.5. Effect of VFe_2O_4@$_{mono}$ZIF-8 on plasma biochemical indices

VFe_2O_4@$_{mono}$ZIF-8 had no significant effect ($P < 0.05$) on the weights and relative weights of organs of the groups that received 1 and 2 mg kg^{-1} of treatment when contrasted with the control group (Table 2). The observation suggests the stability of VFe_2O_4@$_{mono}$ZIF-8 within the biological systems of the experimental animals. Moreover, the animals were stable and no death was recorded for the entire experimental period.

Liver function tests are essential for judging the health status of the liver. For liver assessment, alanine transaminase (ALT) and aspartate transaminase (AST) are enzymes found in liver cells, and elevated levels can indicate liver damage or inflammation. A previous study has shown that elevated levels of the alkaline phosphatase (ALP) enzyme may suggest bile duct obstruction or bone disorders.[77] The effects of VFe_2O_4@$_{mono}$ZIF-8 on plasma liver function indices are shown in Fig. 6. The result showed no significant alterations in the plasma levels of AST, ALT, alkaline phosphatase, direct bilirubin, total bilirubin and albumin when compared to the control ($P < 0.05$). This observation suggests that VFe_2O_4@$_{mono}$ZIF-8 poses no obvious

Table 2 Impact of VFe_2O_4@$_{mono}$ZIF-8 on the organ and relative organ weights of studied animals[a]

Group	LW	RLW	KW	RKW	HW	RHW	SW	RSW	LW	RLW
A	5.86 ± 0.50	2.97 ± 0.25	1.17 ± 0.08	0.59 ± 0.04	0.70 ± 0.06	0.35 ± 0.03	0.62 ± 0.03	0.32 ± 0.02	1.15 ± 0.19	0.58 ± 0.10
B	5.84 ± 0.27	2.96 ± 0.14	1.10 ± 0.06	0.56 ± 0.03	0.64 ± 0.03	0.32 ± 0.02	0.56 ± 0.05	0.28 ± 0.03	1.10 ± 0.05	0.56 ± 0.02
C	5.52 ± 0.35	2.90 ± 0.18	1.18 ± 0.07	0.62 ± 0.03	0.64 ± 0.02	0.34 ± 0.01	0.60 ± 0.04	0.31 ± 0.02	1.20 ± 0.09	0.63 ± 0.04

[a] A = control, B = 1 mg kg^{-1}, C = 2 mg kg^{-1}, LW (g) = liver weight, RLW (g per 100 g body weight) = relative liver weight, KW (g) = kidney weight, RKW (g per 100 g body weight) = relative kidney weight, HW (g) = heart weight, RHW (g per 100 g body weight) = relative heart weight, SW (g) = spleen weight, RSW (g per 100 g body weight) = relative spleen weight, LW (g) = lung weight, and RLW (g per 100 g body weight) = relative lung weight. Each value represents the mean ± standard error of the mean of 5 animals.

 © 2025 The Author(s). Published by the Royal Society of Chemistry

Open Access Article. Published on 05 Desemba 2024. Downloaded on 13/12/2025 21:30:58.
This article is licensed under a Creative Commons Attribution-NonCommercial 3.0 Unported Licence.

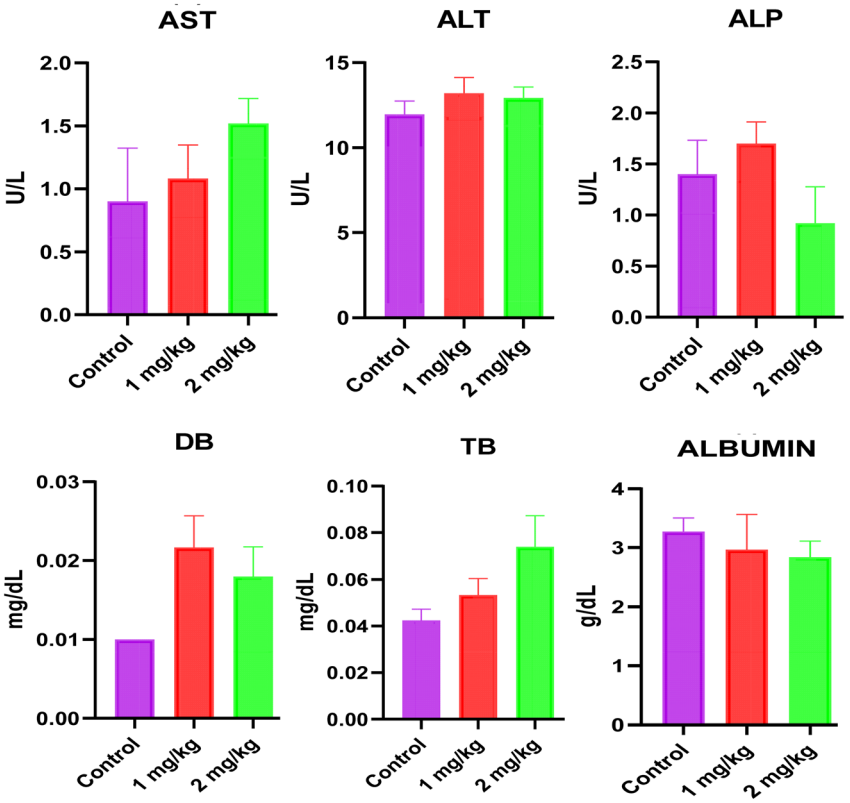

Fig. 6 Effects of $VFe_2O_4@_{mono}ZIF\text{-}8$ on plasma liver function indices. Each value represents the mean ± SEM of 6 animals. AST = aspartate aminotransferase; ALT = alanine amino transferase; ALP = alkaline phosphatase; DB = direct bilirubin; TB = total bilirubin.

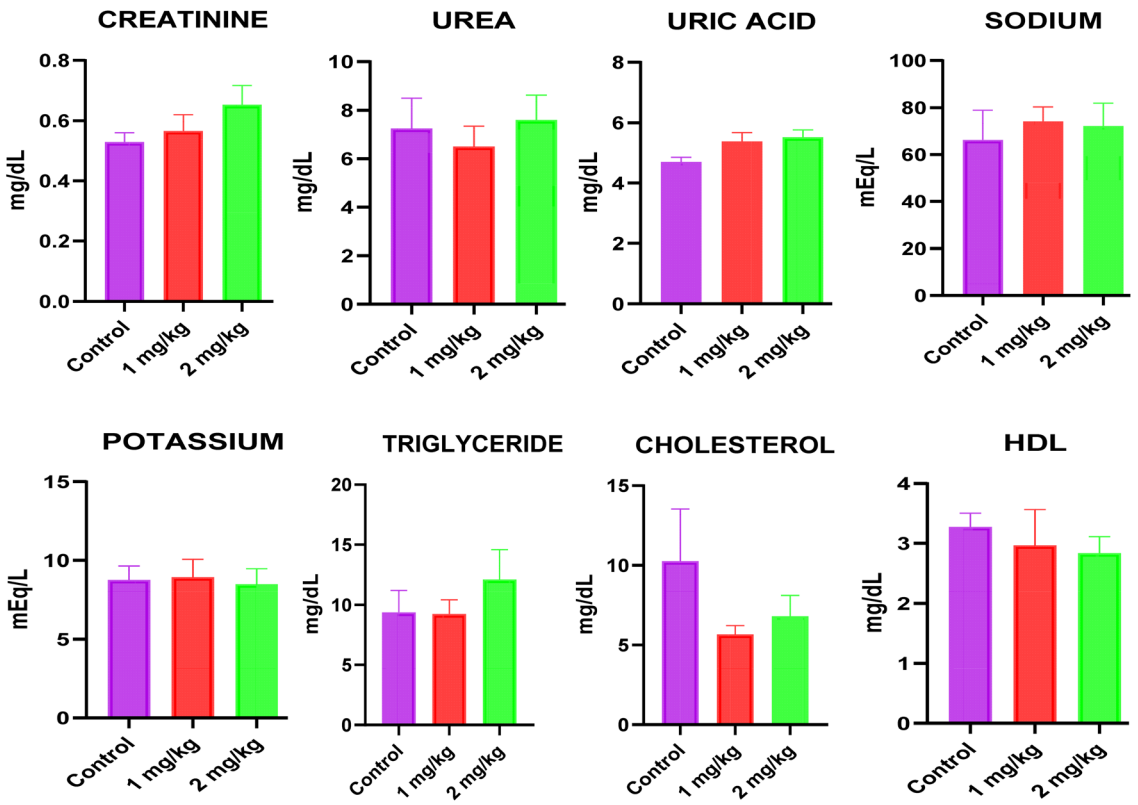

Fig. 7 Effects of $VFe_2O_4@_{mono}ZIF\text{-}8$ on plasma kidney function and plasma lipid profile indices. Each value represents the mean ± SEM of 6 animals.

Open Access Article. Published on 05 Desemba 2024. Downloaded on 13/12/2025 21:30:58.
This article is licensed under a Creative Commons Attribution-NonCommercial 3.0 Unported Licence.

threat to the safety of the studied animals based on the results of the examined biochemical parameters. Similarly, these results are in tandem with those of another study in mice that showed the absence of any significant effects on the liver function markers in animals exposed to the oxides of vanadium nanoparticles in a dose range of 2–6 mg kg^{-1}.[78]

The results of the effect of $VFe_2O_4@_{mono}$ZIF-8 on plasma kidney function parameters are displayed in Fig. 7. The kidney is crucial for filtering and removing waste products, urea, creatinine, and uric acid from the body. Sodium and potassium levels are also closely linked to kidney function. The kidneys are essential for maintaining the balance of these electrolytes, which is crucial for controlling fluid levels, blood pressure, and the proper functioning of nerves and muscles.[79] Evaluating renal function is therefore key to understanding kidney health.[80] In the present study, no significant changes were observed in sodium, potassium, creatinine, urea and uric acid levels in animals that received $VFe_2O_4@_{mono}$ZIF-8 when compared to the control group. A previous study has shown that nanoparticles made of yttrium vanadate doped with europium(III) can reduce toxicity in mouse melanoma models, which was also accompanied by decreases in serum creatinine and urea levels.[81] Interestingly, $VFe_2O_4@_{mono}$ZIF-8 exhibited no significant changes in the plasma creatine, urea and uric acid levels of rats studied, suggesting healthy function of the studied kidneys. Furthermore, there was no significant effect on plasma electrolytes, sodium and potassium levels.

The body is capable of storing triglycerides as a source of energy. However, when triglyceride levels are high, particularly when combined with low high-density lipoprotein (HDL) or

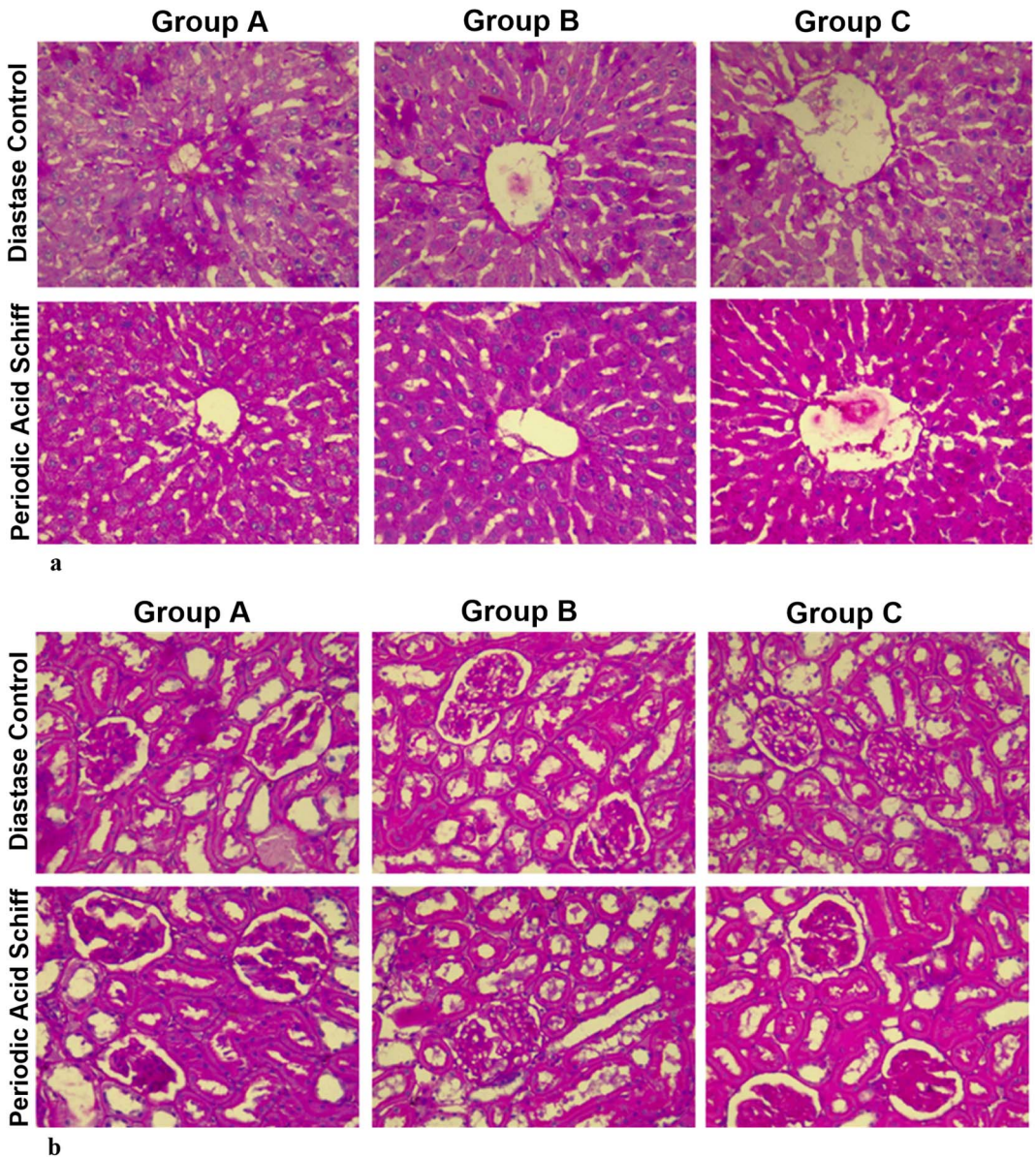

Fig. 8 Photomicrographs of the liver (a) and kidney (b) of a Wistar rat stained with periodic acid–Schiff (X400).

© 2025 The Author(s). Published by the Royal Society of Chemistry

Open Access Article. Published on 05 Desemba 2024. Downloaded on 13/12/2025 21:30:58.
This article is licensed under a Creative Commons Attribution-NonCommercial 3.0 Unported Licence.

high low-density lipoprotein (LDL), the risk of health issues like heart attack increases.[82] Human occupational exposure to vanadium was reported to improve lipid profile atherogenic indices in a previous study.[83] Corroborating this effect, VFe_2O_4@$_{mono}$ZIF-8 elicited no significant changes in plasma cholesterol, HDL and triglyceride levels.

Periodic Acid–Schiff (PAS) is a routine stain in brain, cornea, kidney, liver, and skeletal muscle tissues. Photomicrographs of the liver stained with periodic acid–Schiff (X400) digested with diastase showed positive globules across all groups, which is indicative of alpha-1 antitrypsin within hepatocytes (Fig. 8). Similarly, the photomicrograph of the kidney stained with periodic acid–Schiff (X400) did not reveal any morphological alterations in the glomeruli of groups A and B. However, group C showed mild positive reactivity indicative of tubulitis. The result revealed protein casts in the renal morphology of test rats exposed to the high dose of VFe_2O_4@$_{mono}$ZIF-8 (2 mg per kg body weight). Similar alterations in renal histoarchitecture have also been observed in rats treated with urea modified cobalt ferrite nanoparticles.[34]

4. Conclusion

The development of efficient water treatment techniques is hampered by the emergency of pollutants like antibiotics, which were not envisaged to occur in water when the current water treatment techniques were developed. This study synthesized VFe_2O_4@$_{mono}$ZIF-8 to serve as an efficient photocatalyst for decontaminating CP, AP and EY contaminated water. VFe_2O_4@$_{mono}$ZIF-8 was characterized by FTIR, XRD, UV-visible, EDX, SEM, TEM and TGA. XRD revealed that the crystallite size is 34.32 nm, while the average particle size from the TEM image is 162.32 nm. The SEM image revealed a homogeneous surface composed of hexagonal and irregularly shaped particles. EDX results confirmed C, V, O, Fe and Zn as the constituent elements. The bandgap energy is 2.18 eV. VFe_2O_4@$_{mono}$ZIF-8 completely (100%) photodegraded CP, AP and EY in water, which can be described using a pseudo-1st-order model with rate constants CP ($0.0364\ min^{-1}$) > AP ($0.0168\ min^{-1}$) > EY ($0.0116\ min^{-1}$). The photocatalytic degradation capacity of VFe_2O_4@$_{mono}$ZIF-8 compared favorably with previous studies achieving a regeneration capacity >95%, which suggests that VFe_2O_4@$_{mono}$ZIF-8 is a promising photocatalyst for the removal of antibiotics from water. Toxicological assessment provides the basis for more in-depth studies on the molecular mechanisms underpinning the protective effects of VFe_2O_4@$_{mono}$ZIF-8, paving the way for its industrial commercialization.

Ethical approval

All ethical approvals were obtained from relevant organizations.

Data availability

Data will be provided on request.

Author contributions

Adewale Adewuyi: review & editing, writing – original draft, visualization, software, resources, project administration, methodology, investigation, data curation, and conceptualization; Wuraola B. Akinbola: methodology, investigation, and data curation; Chiagoziem A. Otuechere: review & editing, writing – original draft, visualization, resources, methodology, investigation, data curation, and conceptualization; Adedotun Adesina: methodology, investigation, and data curation; Olaoluwa A. Ogunkunle: methodology, investigation, and data curation; Olamide A. Olalekan: methodology, investigation, and data curation; Sunday O. Ajibade: methodology, investigation, and data curation; Olalere G. Adeyemi: review & editing, writing – original draft, visualization, methodology, investigation, data curation, and conceptualization.

Conflicts of interest

The author declares no competing interests.

Acknowledgements

The authors appreciate the help from the Yusuf Hamied Department of Chemistry, University of Cambridge, UK, and the Department of Chemistry, Obafemi Awolowo University, Ile-Ife, Nigeria.

References

1 H. Q. Anh, T. P. Q. Le, N. Da Le, X. X. Lu, T. T. Duong, J. Garnier, E. Rochelle-Newall, S. Zhang, N.-H. Oh and C. Oeurng, *Sci. Total Environ.*, 2021, **764**, 142865.
2 P. Kairigo, E. Ngumba, L.-R. Sundberg, A. Gachanja and T. Tuhkanen, *Sci. Total Environ.*, 2020, **720**, 137580.
3 O. A. Olalekan, A. J. Campbell, A. Adewuyi, W. J. Lau and O. G. Adeyemi, *Results Chem.*, 2022, **4**, 100457.
4 A. Adewuyi, *Water*, 2020, **12**, 1551.
5 Y. Li, J. Wang, C. Lin, M. Lian, A. Wang, M. He, X. Liu and W. Ouyang, *Environ. Res.*, 2023, **228**, 115827.
6 N. Arabpour and A. Nezamzadeh-Ejhieh, *Process Saf. Environ. Prot.*, 2016, **102**, 431–440.
7 Y. Ben, M. Hu, X. Zhang, S. Wu, M. H. Wong, M. Wang, C. B. Andrews and C. Zheng, *Water Res.*, 2020, **175**, 115699.
8 C. Wang, D. Ye, X. Li, Y. Jia, L. Zhao, S. Liu, J. Xu, J. Du, L. Tian and J. Li, *Environ. Int.*, 2021, **155**, 106651.
9 L. Jiang, W. Zhai, J. Wang, G. Li, Z. Zhou, B. Li and H. Zhuo, *Environ. Res.*, 2023, **239**, 117295.
10 H. Derikvandi and A. Nezamzadeh-Ejhieh, *J. Hazard. Mater.*, 2017, **321**, 629–638.
11 M. Nosuhi and A. Nezamzadeh-Ejhieh, *J. Colloid Interface Sci.*, 2017, **497**, 66–72.
12 E. Shahnazari-Shahrezaie and A. Nezamzadeh-Ejhieh, *RSC Adv.*, 2017, **7**, 14247–14253.
13 R. Kyuchukova, *Bulg. J. Agric. Sci.*, 2020, **26**, 664–668.
14 I. T. Carvalho and L. Santos, *Environ. Int.*, 2016, **94**, 736–757.

Open Access Article. Published on 05 Desemba 2024. Downloaded on 13/12/2025 21:30:58. This article is licensed under a Creative Commons Attribution-NonCommercial 3.0 Unported Licence.

15 A. E. Gahrouei, S. Vakili, A. Zandifar and S. Pourebrahimi, *Environ. Res.*, 2024, 119029.
16 P. Mohammadyari and A. Nezamzadeh-Ejhieh, *RSC Adv.*, 2015, **5**, 75300–75310.
17 A. Kutuzova, T. Dontsova and W. Kwapinski, *Catalysts*, 2021, 728–772.
18 J. Di, J. Xia, M. Ji, H. Li, H. Xu, H. Li and R. Chen, *Nanoscale*, 2015, **7**, 11433–11443.
19 X. Xu, X. Ding, X. Yang, P. Wang, S. Li, Z. Lu and H. Chen, *J. Hazard. Mater.*, 2019, **364**, 691–699.
20 P. Huo, Z. Lu, H. Wang, J. Pan, H. Li, X. Wu, W. Huang and Y. Yan, *Chem. Eng. J.*, 2011, **172**, 615–622.
21 J. Li, F. Liu and Y. Li, *New J. Chem.*, 2018, **42**, 12054–12061.
22 K. Wang, Y. Li, G. Zhang, J. Li and X. Wu, *Appl. Catal. B Environ.*, 2019, **240**, 39–49.
23 A. Yousefi and A. Nezamzadeh-Ejhieh, *Iran. J. Catal.*, 2021, **11**, 247–259.
24 M. Rezaei, A. Nezamzadeh-Ejhieh and A. R. Massah, *Ecotoxicol. Environ. Saf.*, 2024, **269**, 115927.
25 M. Rezaei, A. Nezamzadeh-Ejhieh and A. R. Massah, *ACS Omega*, 2024, **9**, 6093–6127.
26 M. Rezaei, A. Nezamzadeh-Ejhieh and A. R. Massah, *Energy Fuels*, 2024, **38**, 8406–8436.
27 R. Sheikhsamany, A. Nezamzadeh-Ejhieh and R. S. Varma, *Surf. Interfaces*, 2024, **54**, 105205.
28 R. Sheikhsamany and A. Nezamzadeh-Ejhieh, *J. Mol. Liq.*, 2024, 126265.
29 S. Zhou, L. Lu, D. Liu, J. Wang, H. Sakiyama, M. Muddassir, A. Nezamzadeh-Ejhieh and J. Liu, *CrystEngComm*, 2021, **23**, 8043–8052.
30 J. Chen, Z. Zhang, J. Ma, A. Nezamzadeh-Ejhieh, C. Lu, Y. Pan, J. Liu and Z. Bai, *Dalton Trans.*, 2023, **52**, 6226–6238.
31 Z. Lin, D. Liao, C. Jiang, A. Nezamzadeh-Ejhieh, M. Zheng, H. Yuan, J. Liu, H. Song and C. Lu, *RSC Med. Chem.*, 2023, **14**, 1914–1933.
32 M. Li, Z. Zhang, Y. Yu, H. Yuan, A. Nezamzadeh-Ejhieh, J. Liu, Y. Pan and Q. Lan, *Mater. Adv.*, 2023, **4**, 5050–5093.
33 J.-Q. Liu, L. Deng, Y. Qiu, Y. Zhang, J. Zou, A. Kumar, Y. Pan, A. Nezamzadeh-Ejhieh and X. Liu, *RSC Med. Chem.*, 2024, **15**, 2601–2621.
34 A. Adewuyi, C. A. Otuechere, C. A. Gervasi, A. T. Olukanni, E. Yawson, A. A. Rubert and M. V. Mirífico, *J. Mol. Liq.*, 2022, **365**, 120224.
35 A. Adewuyi, C. A. Otuechere, O. L. Adebayo, M. Oyeka and C. Adewole, *Sci. Afr.*, 2021, **14**, e01025.
36 A. Nikhil, D. Thomas, S. Amulya, S. M. Raj and D. Kumaresan, *Sol. Energy*, 2014, **106**, 109–117.
37 Y. Zhang and Y. Jia, *RSC Adv.*, 2018, **8**, 31471–31477.
38 A. Adewuyi and R. A. Oderinde, *Biomass Convers. Biorefin.*, 2022, 1–15.
39 P. Sivakumar, R. Ramesh, A. Ramanand, S. Ponnusamy and C. Muthamizhchelvan, *Mater. Lett.*, 2011, **65**, 483–485.
40 P. Sivakumar, R. Ramesh, A. Ramanand, S. Ponnusamy and C. Muthamizhchelvan, *Appl. Surf. Sci.*, 2012, **258**, 6648–6652.
41 M. Ahmed, Y. M. Al-Hadeethi, A. Alshahrie, A. T. Kutbee, E. R. Shaaban and A. F. Al-Hossainy, *Polymers*, 2021, **13**, 4051.
42 C. Hammond, *The Basics of Crystallography and Diffraction*, Oxford University Press, USA, 2015.
43 D. Gherca, A. Pui, N. Cornei, A. Cojocariu, V. Nica and O. Caltun, *J. Magn. Magn. Mater.*, 2012, **324**, 3906–3911.
44 K. Nadeem, M. Shahid and M. Mumtaz, *Prog. Nat. Sci.:Mater. Int.*, 2014, **24**, 199–204.
45 N. A. Hassan Mohamed, R. N. Shamma, S. Elagroudy and A. Adewuyi, *Resources*, 2022, **11**, 81.
46 E. Casbeer, V. K. Sharma and X.-Z. Li, *Sep. Purif. Technol.*, 2012, **87**, 1–14.
47 A. Adewuyi, *Environ. Nanotechnol., Monit. Manage.*, 2023, 100829.
48 M. Farsi and A. Nezamzadeh-Ejhieh, *Surf. Interfaces*, 2022, **32**, 102148.
49 H. Derikvandi and A. Nezamzadeh-Ejhieh, *J. Photochem. Photobiol., A*, 2017, **348**, 68–78.
50 F. Soleimani and A. Nezamzadeh-Ejhieh, *J. Mater. Res. Technol.*, 2020, **9**, 16237–16251.
51 K. T. Amakiri, A. Angelis-Dimakis and A. Ramirez Canon, *Water Sci. Technol.*, 2022, **85**, 769–788.
52 S. A. Mirsalari and A. Nezamzadeh-Ejhieh, *Sep. Purif. Technol.*, 2020, **250**, 117235.
53 S. Senobari and A. Nezamzadeh-Ejhieh, *Spectrochim. Acta Mol. Biomol. Spectrosc.*, 2018, **196**, 334–343.
54 P. Hemmatpour and A. Nezamzadeh-Ejhieh, *Chemosphere*, 2022, **307**, 135925.
55 A. Morone, P. Mulay and S. P. Kamble, *Pharmaceuticals and Personal Care Products: Waste Management and Treatment Technology*, 2019, pp. 173–212.
56 T. Singh, A. Bhatiya, P. Mishra and N. Srivastava, in *Abatement of Environmental Pollutants*, Elsevier, 2020, pp. 203–243.
57 D. C. da Silva Alves, B. S. de Farias, C. Breslin, L. A. de Almeida Pinto and T. R. S. A. C. Junior, in *Advanced Materials for Sustainable Environmental Remediation*, Elsevier, 2022, pp. 475–513.
58 C.-K. Tsai, C.-H. Huang, J.-J. Horng, H. L. Ong and R.-A. Doong, *Nanomaterials*, 2023, **13**, 282.
59 R. Noroozi, M. Gholami, V. Oskoei, M. Hesami Arani, S. A. Mousavifard, B. Nguyen Le and M. Fattahi, *Sci. Rep.*, 2023, **13**, 16287.
60 A. C. B. Queiróz, A. P. Santos, T. S. Queiroz, A. E. Lima, R. M. P. da Silva, R. A. Antunes, G. E. Luz Jr, A. G. D. Santos and V. P. Caldeira, *Water, Air, Soil Pollut.*, 2023, **234**, 415.
61 W. D. Santos, M. M. Teixeira, I. R. Campos, R. B. de Lima, A. Mantilla, J. A. Osajima, A. S. de Menezes, D. Manzani, A. Rojas and A. C. Alcântara, *Microporous Mesoporous Mater.*, 2023, **359**, 112657.
62 B. Zhu, D. Song, T. Jia, W. Sun, D. Wang, L. Wang, J. Guo, L. Jin, L. Zhang and H. Tao, *ACS Omega*, 2021, **6**, 1647–1656.
63 T. J. Al-Musawi, N. Mengelizadeh, A. I. Alwared, D. Balarak and R. Sabaghi, *Environ. Sci. Pollut. Res.*, 2023, **30**, 70076–70093.
64 P. S. Selvamani, J. J. Vijaya, L. J. Kennedy, A. Mustafa, M. Bououdina, P. J. Sophia and R. J. Ramalingam, *Ceram. Int.*, 2021, **47**, 4226–4237.

© 2025 The Author(s). Published by the Royal Society of Chemistry

Open Access Article. Published on 05 Desemba 2024. Downloaded on 13/12/2025 21:30:58.
This article is licensed under a Creative Commons Attribution-NonCommercial 3.0 Unported Licence.

65 L. Wolski, K. Grzelak, M. Muńko, M. Frankowski, T. Grzyb and G. Nowaczyk, *Appl. Surf. Sci.*, 2021, **563**, 150338.
66 D. Van Thuan, T. B. Nguyen, T. H. Pham, J. Kim, T. T. H. Chu, M. V. Nguyen, K. D. Nguyen, W. A. Al-Onazi and M. S. Elshikh, *Chemosphere*, 2022, **308**, 136408.
67 X.-J. Wen, C.-G. Niu, L. Zhang, C. Liang, H. Guo and G.-M. Zeng, *J. Catal.*, 2018, **358**, 141–154.
68 J. Ren, S. Ni, Y. Shen, D. Niu, R. Sun, C. Wang, L. Deng, Q. Zhang, Y. Tang and X. Jiang, *J. Cleaner Prod.*, 2022, **379**, 134758.
69 K. Vignesh, M. Rajarajan and A. Suganthi, *Mater. Sci. Semicond. Process.*, 2014, **23**, 98–103.
70 G. Li, B. Wang, J. Zhang, R. Wang and H. Liu, *Appl. Surf. Sci.*, 2019, **478**, 1056–1064.
71 L. Albornoz, S. da Silva, J. P. Bortolozzi, E. D. Banus, P. Brussino, M. Ulla and A. M. Bernardes, *Chemosphere*, 2021, **268**, 128858.
72 N. A. H. Mohammed, R. N. Shamma, S. Elagroudy and A. Adewuyi, *Results Chem.*, 2024, **7**, 101307.
73 T. J. Al-Musawi, P. Rajiv, N. Mengelizadeh, F. S. Arghavan and D. Balarak, *J. Mol. Liq.*, 2021, **337**, 116470.
74 M. G. Alalm, S. Ookawara, D. Fukushi, A. Sato and A. Tawfik, *J. Hazard. Mater.*, 2016, **302**, 225–231.
75 S. Sohrabnezhad, A. Pourahmad and M. F. Karimi, *J. Solid State Chem.*, 2020, **288**, 121420.
76 A. Fakhri, S. Rashidi, I. Tyagi, S. Agarwal and V. K. Gupta, *J. Mol. Liq.*, 2016, **214**, 378–383.
77 V. Lala, M. Zubair and D. Minter, Liver function test, *StatPearls*, 2023, pp. 1–5.
78 E.-J. Park, G.-H. Lee, C. Yoon and D.-W. Kim, *Environ. Res.*, 2016, **150**, 154–165.
79 I. Shrimanker and S. Bhattarai, Electrolyte, *StatPearls*, 2019, pp. 1–6.
80 W. G. Miller and L. A. Inker, *Contemporary Practice in Clinical Chemistry*, 2020, pp. 611–628.
81 N. H. Ferreira, R. A. Furtado, A. B. Ribeiro, P. F. de Oliveira, S. D. Ozelin, L. D. R. de Souza, F. R. Neto, B. A. Miura, G. M. Magalhães and E. J. Nassar, *J. Inorg. Biochem.*, 2018, **182**, 9–17.
82 K. Hajian-Tilaki, B. Heidari and A. Bakhtiari, *Caspian J. Intern. Med.*, 2020, **11**, 53.
83 Y. Zhang, Q. Zhang, C. Feng, X. Ren, H. Li, K. He, F. Wang, D. Zhou and Y. Lan, *Lipids Health Dis.*, 2014, **13**, 1–6.

© 2025 The Author(s). Published by the Royal Society of Chemistry